Panel Method for 3D Inviscid Flow Simulation of Shrouded Fans with Tip-Leakage Flow

Valentin Caries, Jérôme Boudet, Eric Lippinois

MDPI

Article

Panel Method for 3D Inviscid Flow Simulation of Shrouded Fans with Tip-Leakage Flow

Valentin Caries [1,2,*], Jérôme Boudet [1] and Eric Lippinois [2]

[1] Ecole Centrale de Lyon, CNRS, Universite Claude Bernard Lyon 1, INSA Lyon, LMFA, UMR5509, 69130, Ecully, France; valentin.caries@ec-lyon.fr (V.C.); jerome.boudet@ec-lyon.fr (J.B.)
[2] Safran Aircraft Engines, Moissy-Cramayel, France; valentin.caries@ec-lyon.fr (V.C.); eric.lippinois@safrangroup.com (E.L.)
* Correspondence: valentin.caries@ec-lyon.fr (V.C.);

Abstract: This paper presents a low-order three-dimensional approach for predicting the inviscid flow around shrouded fans. The method is suitable for early design stages and allows a broad exploration of design possibilities at minimal cost. It combines the vortex lattice method with the panel method by using a mixed boundary condition. In addition, it models the tip-leakage flow using an iterative algorithm. First, the verification of the approach is carried out on a shrouded fan configuration. The wake length is a decisive parameter for ensuring correct flow deflection in shrouded applications. A periodicity condition is introduced and validated, which reduces the computational and memory requirements. On average, the calculations take less than one minute in real time. The approach is validated on the same shrouded fan configuration. A good agreement is obtained with RANS concerning the mean flow and the tip-leakage flow characteristics. Sensitivity to the mass flow rate is also fairly well predicted, although discrepancies develop at lower mass flow rates.

Keywords: Panel Method, Vortex Lattice Method, Shrouded Fan, Tip-Leakage Flow

1. Introduction

The design of a modern fan confronts manufacturers with major challenges. Minimizing aerodynamic losses is crucial for improving propulsion efficiency and reducing specific fuel consumption. Accurate prediction of the physical phenomena involved in each design iteration is essential. Tool versatility is imperative to account for disruptive geometries while ensuring precision and robustness. The aerodynamic design process for new blade geometries is complicated and involves different levels of modeling fidelity, including one-dimensional, through-flow and three-dimensional approaches. Moreover, the emergence of new loss reduction technologies poses significant challenges to traditional modeling methods. Low-order techniques, often relying on correlations from limited experimental data, can deviate from intended designs. Reynolds-averaged Navier-Stokes (RANS) simulations, which use turbulence models based on elementary configurations, run the risk of incorrectly predicting vortex structures and exhibiting unphysical behaviors. As a result, high-fidelity methods such as the large-eddy simulation and derived approaches are gaining traction, but are hampered by their high computational cost, which limits their use in the early stages of design. To mitigate the limitations of low-order methods, it may prove advantageous to use models based on general equations rather than correlations. This facilitates the iterative exploration of new geometries and aerodynamic conditions, and leads to reliable predictions throughout the design process. Empirical correlations should be focused on elementary phenomena, thus controlling the model limits.

Panel methods have been used extensively in both aeronautical and marine engineering to analyze the potential flow around lifting objects. These low-order methods, based on singularity theory [1], provide efficient means of predicting aerodynamic performance,

Citation: Caries, V.; Boudet, J.; Lippinois, E. Panel Method for 3D Inviscid Flow Simulation of Shrouded Fans with Tip-Leakage Flow. *Int. J. Turbomach. Propuls. Power* **2024**, *1*, 0. https://doi.org/

Received:
Revised:
Accepted:
Published:

induced drag, lift distribution and surface interactions. Among the various panel methods available, the vortex lattice method (VLM) and the so-called panel method are discussed here.

The VLM, which was developed in the 1930s as an extension of Prandtl's lifting line theory [2], discretizes the surface in the chord and span directions with vortex singularities. This approach enables the solution of 3D potential flows around bodies with low aspect ratios. In this method, the thickness is not modeled, and the singularities are concentrated on a mean surface, typically the camber of a blade. The VLM was widely used between the 1960s and 1980s and offered significant advantages in terms of memory and computational cost. Studies on propellers showed the versatility of the VLM in various configurations. Helical horseshoe vortices were developed to model the wake [3,4]. Counter-rotating propellers and ducted propellers have been simulated [5–8]. Recent advances have extended the applicability of the VLM to propellers with different angles of incidence or unsteady flows [9,10]. Coupled with Lagrangian solvers, it accurately solves wakes generated by drone rotors [11]. Modern software address various external aerodynamic challenges [12], including phenomena such as aircraft installation effects [13].

The panel method differs by considering the actual blade geometry, including thickness, and comprehensively addresses lifting problems with doublets and source singularities. In the context of propellers, it has evolved to include source singularities for endwall modeling [6]. Recent advances [14–18] even include duct modeling in addition to iterative wake models and tip-leakage flow (TLF) considerations.

Combining the benefits of both approaches involves using a mixed boundary condition [1]. An example of application was shown with an unsteady computation on a full plane [19]. The VLM is used to represent lifting components such as wings, tails and canards, which are assumed to be thin. The panel method models the fuselage and other non-lifting components. The computational cost is reduced compared to using only the panel method, while still accounting for the effects of the non-lifting components on the aircraft. This method also provided accurate results in the context of turbomachinery where a linear cascade was confined in a computational box, effectively isolating the external fictitious flow from the simulated internal flow [20].

These studies highlight the efficiency of the VLM and the panel method in capturing intricate flow phenomena in propellers, and make it a valuable tool for performance evaluation and design optimization. However, as far as the authors are aware, the method has never been applied to model a shrouded fan with tip-leakage flow. In this work, a mixed approach, named hybrid panel method (HPM), is used to model the potential flow around a shrouded fan.

2. Numerical methods

2.1. General equations

Panel methods calculate the aerodynamic field around bodies in steady, inviscid, irrotational and incompressible flow conditions. The velocity vector is defined by the velocity potential: $\mathbf{Q} = \nabla\Phi$. The Laplace equation is solved in the inertial reference frame of the body:

$$\nabla^2\Phi = 0 \tag{1}$$

Elementary solutions, so-called singularities, which are distributed over the walls of the domain, are used to solve the problem. Three boundary conditions are required. First, the far-field boundary condition, which states that the flow disturbance decreases far away from the body:

$$\lim_{r\to\infty} \nabla\Phi = 0 \tag{2}$$

This condition is always fulfilled due to the mathematical definition of the singularities. Second, the condition of non-penetration ensures that the normal velocity of the wall in the body reference frame is zero:

$$\nabla(\Phi + \Phi_\infty) \cdot \mathbf{n} = 0 \tag{3}$$

Where Φ_∞ is the velocity potential of the free flow relative to the body and $\mathbf{n}$ is the normal vector of the body surface. There are two types of non-penetration condition: the Neumann condition, which refers to the velocity components as in Equation (3), and the Dirichlet condition, which refers to the velocity potential:

$$(\Phi + \Phi_\infty)_i = cst \tag{4}$$

The subscript i stands for the potential inside the body. The former type of condition is used in VLM and considers zero-thickness surfaces, while the latter is employed in the panel method and refers to the actual thick geometry. The present approach combines both types of boundary conditions to leverage their advantages. Third, the Kutta condition requires a smooth flow at the trailing edge (TE) of the blade with a finite velocity. Therefore, a sharp TE with a known position of detachment and a wake are required. It leads to a zero circulation at the TE:

$$\gamma_{TE} = 0 \tag{5}$$

This condition ensures the unicity of the solution. The wake is usually modeled by a meshed vortex sheet in which the pressure difference between the two sides of each panel must be zero. This slip condition results in the wake being parallel to the flow. Either unsteady approaches [11,12,19] or iterative approaches [14] achieve this. To reduce the computational effort, the current approach assumes that the wake geometry is frozen and defined beforehand. To prevent important errors, a model for generating the wake geometry is considered later.

2.2. Hybrid Panel Method

2.2.1. Singularities

To calculate the flow around a shrouded fan, the HPM must take into account a row of blades, a hub and a shroud. Figure 1 shows the mapping of singularities onto the walls of the domain. The strategy to leverage the VLM and the panel method involves the following steps. The former approach uses vortex rings with intensity Γ. They discretize the hub and the shroud, which are modeled as thin bodies. Their corresponding wakes are also broken down into vortex rings. To account for thickness effects, the blade and its tip are modeled with the panel method. Quadrilateral sources and doublets with constant strengths σ and μ are employed. Since quadrilateral doublets are equivalent to vortex rings [1], they are used to model the blade wake and the TLF vortex sheet.

The sources are crucial for the non-penetration, as they counteract the incident flow at the leading edge (LE). To avoid the introduction of additional unknowns, each quadrilateral source has a fixed intensity:

$$\sigma = \mathbf{n} \cdot \mathbf{Q}_{rel} \tag{6}$$

Where $\mathbf{Q}_{rel}$ represents the relative freestream velocity vector at the panel center and is calculated as:

$$\mathbf{Q}_{rel} = \mathbf{Q}_\infty - \mathbf{\Omega} \times \mathbf{r}, \quad \mathbf{Q}_\infty = Q_\infty \begin{pmatrix} \cos\alpha \cos\varphi \\ \cos\alpha \sin\varphi \\ \sin\alpha \end{pmatrix} \tag{7}$$

r is the radial coordinate vector of the panel center, $\mathbf{\Omega}$ the angular velocity of the rotor and $\mathbf{Q}_\infty$ the free flow velocity vector of amplitude Q_∞, azimuthal angle α and radial angle φ. This alleviates the doublet intensities and improves the numerical stability.

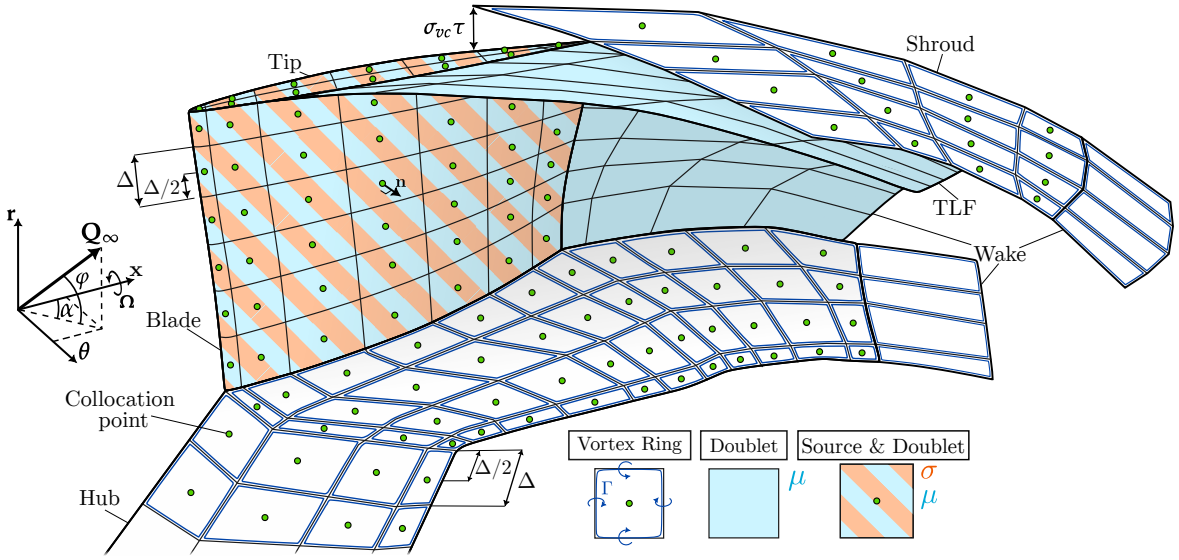

Figure 1. Principle of HPM: singularities and collocation points mapping.

2.2.2. Non-penetration condition

The HPM combines the Neumann condition of the VLM with the Dirichlet condition of the panel method. Let n_{ew} be the number of endwall panels with the Neumann boundary condition and n_b the number of blade panels with the Dirichlet boundary condition. Furthermore, let $n_{ew,\omega}$ be the number of endwall wake panels and $n_{b,\omega}$ the number of panels for the blade wake and the TLF sheet. The non-penetration condition is applied at each collocation point i located at the center of each panel. The linear system is given by:

$$\begin{cases} \sum_{j=1}^{n_{ew}} a_{v_{ij}}^{\perp}\Gamma_j + \sum_{l=1}^{n_{ew,\omega}} a_{v_{il}}^{\perp}\Gamma_l + \sum_{j=1}^{n_b} c_{v_{ij}}^{\perp}\mu_j + \sum_{l=1}^{n_{b,\omega}} c_{v_{il}}^{\perp}\mu_l = -\mathbf{Q}_{rel_i}\cdot\mathbf{n}_i - \sum_{j=1}^{n_b} b_{v_{ij}}^{\perp}\sigma_j \\ \sum_{j=1}^{n_{ew}} a_{p_{ij}}\Gamma_j + \sum_{l=1}^{n_{ew,\omega}} a_{p_{il}}\Gamma_l + \sum_{j=1}^{n_b} c_{p_{ij}}\mu_j + \sum_{l=1}^{n_{b,\omega}} c_{p_{il}}\mu_l = -\sum_{j=1}^{n_b} b_{p_{ij}}\sigma_j \end{cases} \tag{8}$$

The first equation represents the Neumann boundary condition (Equation (3)). It applies to collocation points on the hub and the shroud. The second equation refers to the Dirichlet boundary condition (Equation (4)). It applies to the blade and the tip collocation points. The equations for the velocity components (denoted by v) and the potential (denoted by p), which include the vortex influence a, the source influence b and the doublet influence c, are described in detail in [1,21]. The superscript $\perp$ indicates that the velocity components are projected onto the normal vector $\mathbf{n}$ at the collocation point i.

A common approach to accelerate computations consists in separating far-field and near-field contributions [1,20]. The former employs punctual singularity formulations, while the latter uses quadrilateral doublets and sources. Near-field formulation are used when the distance is lower than 3 characteristic length of the panel.

2.2.3. Kutta condition

The Kutta condition (Equation (5)) is explicitly enforced thanks to additional equations. The Kutta conditions on the blade TE, the blade tip and the endwall TE control the intensities of the blade wake, the TLF sheet and the endwall wakes, respectively. For each streamwise wake panel row, in order to satisfy the Helmholtz's theorems, the intensities

of the singularities are considered constant. The total influence of each wake panel row is determined by summing the influences of the singularities within that row. Consequently, only the streamwise vertices have a significant effect on the result, while the influence of the cross-flow vertices is canceled from one panel to another. This method allows a piecewise evaluation of complex wake shapes, which is essential for annular configurations.

The Kutta condition for an endwall wake is given by:

$$\Gamma_\omega = -\Gamma_{ew,TE} \tag{9}$$

Γ_ω represents the circulation of a given endwall wake row, while $\Gamma_{ew,TE}$ represents the circulation of the corresponding vortex ring at the TE of the endwall. For the blade wake, it writes:

$$\mu_\omega = \mu_{SS,TE} - \mu_{PS,TE} \tag{10}$$

μ_ω represents the doublet intensity of a given blade wake row. $\mu_{SS,TE}$ and $\mu_{PS,TE}$ denote the doublet intensities at the corresponding TE for the suction side and pressure side panels, respectively. Lastly, for the TLF sheet, the Kutta condition is expressed by:

$$\mu_{TLF} = \mu_{SS,tip} - \mu_{PS,tip} \tag{11}$$

μ_{TLF} corresponds to the doublet intensity of a given TLF sheet row. $\mu_{SS,tip}$ and $\mu_{PS,tip}$ refer to the doublet intensities at the tip for the corresponding suction side and pressure side panels, respectively.

These three equations do not introduce new unknowns in the linear system. They just add an extra term to the influence coefficients related to the singularities on the body edges that connect to each wake. Regarding the vortex rings on the TE of the endwalls, the corrected influence coefficients, accounting for the Kutta condition, are given by:

$$a^{\perp *}_{v_{ij}} = a^{\perp}_{v_{ij}} + a^{\perp}_{v_{il}}, \quad a^{*}_{p_{ij}} = a_{p_{ij}} + a_{p_{il}} \tag{12}$$

Where the subscript j refers to the vortex ring at the endwall TE while l denotes the corresponding vortex ring in the wake. In the same way, for the doublet on the TE and tip edges of the blade, the following corrections apply:

$$c^{\perp *}_{v_{ij}} = c^{\perp}_{v_{ij}} \pm c^{\perp}_{v_{il}}, \quad c^{*}_{p_{ij}} = c_{p_{ij}} \pm c_{p_{il}} \tag{13}$$

Here, the subscript j refers to the doublet at the blade TE while l denotes the corresponding doublet in the wake or the TLF sheet. The sign depends on the normal orientation of each panel.

2.2.4. Periodicity condition

For cases with numerous periodic blades around the circumference, the size of the linear system can be large. This can lead to a significant increase in computational and memory requirements, which reduces the interest of this low-order method. The periodicity condition proposed originally for the VLM [22] is extended to the HPM. Assuming that the flow around each blade is identical, the method solves the linear system of Equation (8) for only one sector. The other $N-1$ periodic sectors are taken into account when calculating the influence coefficients. The linear system is then written as follows:

$$\begin{cases} \sum_{k=1}^{N} \left(\sum_{j=1}^{n_{ew}^{(1)}} a_{v_{ij}}^{\perp(k)} \Gamma_j^{(1)} + \sum_{l=1}^{n_{ew,\omega}^{(1)}} a_{v_{il}}^{\perp(k)} \Gamma_l^{(1)} + \sum_{j=1}^{n_b^{(1)}} c_{v_{ij}}^{\perp(k)} \mu_j^{(1)} + \sum_{l=1}^{n_{b,\omega}^{(1)}} c_{v_{il}}^{\perp(k)} \mu_l^{(1)} \right) \\ \qquad = -\mathbf{Q}_{rel_i}^{(1)} \cdot \mathbf{n}_i^{(1)} - \sum_{k=1}^{N} \sum_{j=1}^{n_b^{(1)}} b_{v_{ij}}^{\perp(k)} \sigma_j^{(1)} \\ \sum_{k=1}^{N} \left(\sum_{j=1}^{n_{ew}^{(1)}} a_{p_{ij}}^{(k)} \Gamma_j^{(1)} + \sum_{l=1}^{n_{ew,\omega}^{(1)}} a_{p_{il}}^{(k)} \Gamma_l^{(1)} + \sum_{j=1}^{n_b^{(1)}} c_{p_{ij}}^{(k)} \mu_j^{(1)} + \sum_{l=1}^{b,n_\omega^{(1)}} c_{p_{il}}^{(k)} \mu_l^{(1)} \right) \\ \qquad = -\sum_{k=1}^{N} \sum_{j=1}^{n_b^{(1)}} b_{p_{ij}}^{(k)} \sigma_j^{(1)} \end{cases} \tag{14}$$

This approach reduces the size of the linear system by a factor of N^2 compared to a complete blade row calculation. In addition, the cost for calculating the influence coefficients is lower, as it only concerns the influence of the periodic sectors on the solved sector. The cross influences between the periodic sectors are neglected. Since the mesh is only required for a single sector, the memory cost of the simulation is also minimized.

2.2.5. Linear system

In view of these considerations, the resulting linear system can be expressed in matrix and vector notation as follows:

$$\begin{pmatrix} a_{v_{11}}^{\perp} & \cdots & a_{v_{1n_{ew}}}^{\perp} & c_{v_{11}}^{\perp} & \cdots & c_{v_{1n_b}}^{\perp} \\ \vdots & \ddots & \vdots & \vdots & \ddots & \vdots \\ a_{v_{n_{ew}1}}^{\perp} & \cdots & a_{v_{n_{ew}n_{ew}}}^{\perp} & c_{v_{n_b1}}^{\perp} & \cdots & c_{v_{n_bn_b}}^{\perp} \\ a_{p_{11}} & \cdots & a_{p_{1n_{ew}}} & c_{p_{11}} & \cdots & c_{p_{1n_b}} \\ \vdots & \ddots & \vdots & \vdots & \ddots & \vdots \\ a_{p_{n_{ew}1}} & \cdots & a_{p_{n_{ew}n_{ew}}} & c_{p_{n_b1}} & \cdots & c_{p_{n_bn_b}} \end{pmatrix} \begin{pmatrix} \Gamma_1 \\ \vdots \\ \Gamma_{n_{ew}} \\ \mu_1 \\ \vdots \\ \mu_{n_b} \end{pmatrix} = - \begin{pmatrix} \mathbf{Q}_{rel_1} \cdot \mathbf{n}_1 + \sum_{j=1}^{n_b} b_{v_{1j}}^{\perp} \sigma_j \\ \vdots \\ \mathbf{Q}_{rel_{n_{ew}}} \cdot \mathbf{n}_{n_{ew}} + \sum_{j=1}^{n_b} b_{v_{n_{ew}j}}^{\perp} \sigma_j \\ \sum_{j=1}^{n_b} b_{p_{1j}} \sigma_j \\ \vdots \\ \sum_{j=1}^{n_b} b_{p_{n_bj}} \sigma_j \end{pmatrix} \tag{15}$$

The unknowns of the system consist of the circulations on the endwalls and the doublet intensities on the blade and the TLF sheet. The structure of the linear system shows that the diagonal blocks are derived from the VLM for the endwalls and from the panel method for the blade and the TLF. The extra-diagonal blocks calculate the cross-influences. The right-hand side of the linear system covers the incoming freestream flow and the influence of the sources on the solved sector.

2.2.6. Post-processing

After solving the linear system, the aerodynamic field can be reconstructed over the domain by summing the influences of the singularities with known intensities. The flow velocity at the surface of a blade panel in its own reference frame is given by:

$$\mathbf{Q} = \left(-\frac{\partial \mu}{\partial l}, -\frac{\partial \mu}{\partial m}, \sigma \right)_{(\mathbf{l},\mathbf{m},\mathbf{n})} \tag{16}$$

Here, ∂l and ∂m are the distances between two collocation points in the local reference frame of the panel, namely in the direction of the flow and perpendicularly. Expressing the relative velocity vector of the panel center in the local reference frame, the pressure coefficient is given by:

$$C_p = 1 - \left(\frac{\mathbf{Q}_{rel} + \mathbf{Q}}{\mathbf{Q}_{rel}} \right)^2 \tag{17}$$

The pitchwise force coefficient c_z is then calculated by integrating the pressure coefficient over the chordwise direction.

2.3. Geometry and mesh considerations

This section describes the process of generating the geometry and the structured surface mesh compatible with HPM, inspired by the method of Baltazar et al. [14]. Figure 2 illustrates the meshing approach.

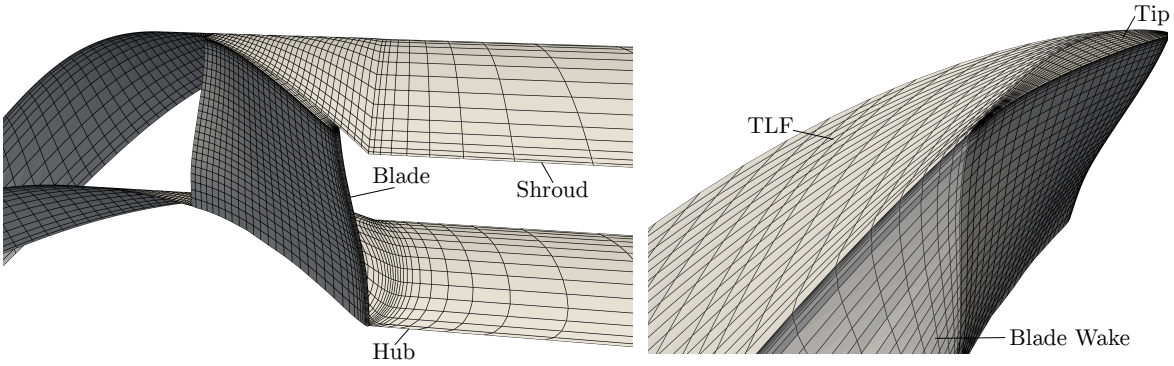

Figure 2. Geometry and mesh for the HPM. Left: the solid walls without the wakes and the TLF. Right: blade, wake and TLF (the endwalls are not shown).

2.3.1. Endwalls

The hub and shroud are divided into three sections. From the inlet to the blade LE, the mesh is aligned with the freestream flow with a cosine clustering near the LE. Between the LE and the TE, the hub mesh refines around the blade walls to capture the circulation gradients. For the shroud, the mesh is aligned with the stagger angle of the blade tip for numerical stability. From the blade TE to the outlet, the mesh follows the blade wake direction at the root and tip, with a helical path and cosine clustering near the TE. Figure 3 illustrates how this method reduces the unphysical interactions between the quadrilateral doublets of the blade wake and the endwall collocation points. The edges of these doublets form singularity lines. Avoiding intersections with collocation points prevents unwanted behaviors on the endwalls. This in turn ensures the accuracy of the blade results. The axial extent of the endwalls is adjusted to reduce the artificial influence of their LE and TE on the blade row. As a result, both ends are located 10 axial chords away from the blade.

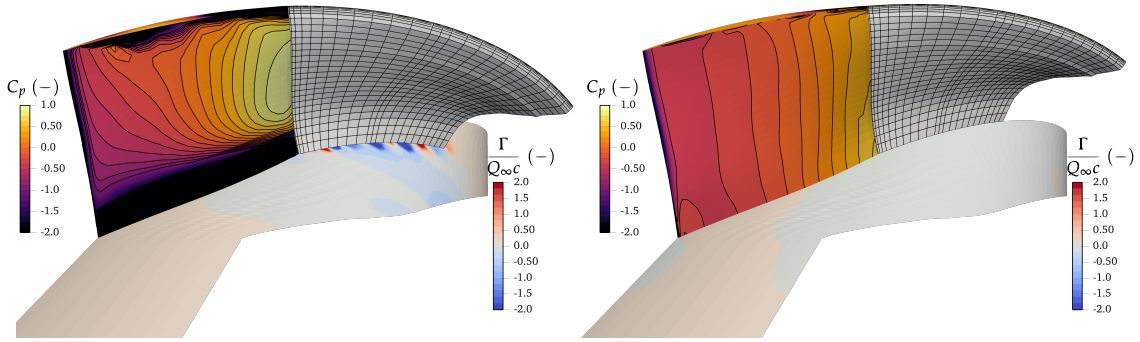

Figure 3. Influence of the alignement of the hub and wake meshes. Left: no alignment. Right: hub mesh aligned with the blade wake direction. The pressure coefficient C_p is shown on the blade, and the normalized circulation on the hub.

2.3.2. Blade

The blade with a sharp TE is meshed, increasing its height to account for the recirculation bubble near the pressure side edge in the tip gap. The size of the tip gap is reduced by a factor $1 - \sigma_{vc} = 1 - \frac{\pi}{\pi+2} \approx 0.389$, which corresponds to the theoretical contraction coefficient of the vena contracta [23]. Experimental measurements are in close agreement with this value [24]. Mesh refinement follows the guidelines of Montsarrat [25]. It ensures convergence at the blade tip:

$$\frac{\tau}{\Delta_0} > 2 \tag{18}$$

Here, τ is the size of the tip gap and Δ_0 is the height of the first panel row at the tip of the blade tip. The sharp TE leads to triangular panels on the blade tip, which modify the equations for the influence coefficients as described in [1,26].

2.3.3. Wakes and TLF sheet

The endwall wakes are aligned with the respective endwalls and have a length of 10 axial blade chords to minimize the unwanted influence of their starting vortex on the blade row. The blade wake follows a helical path with a pitch angle varying with radius. As shown on Figure 4, it is aligned with the TE bisector. This aims to estimate the orientation of the wake in relation to the downstream flow. This helps to minimize the errors in slip condition caused by the frozen wake method.

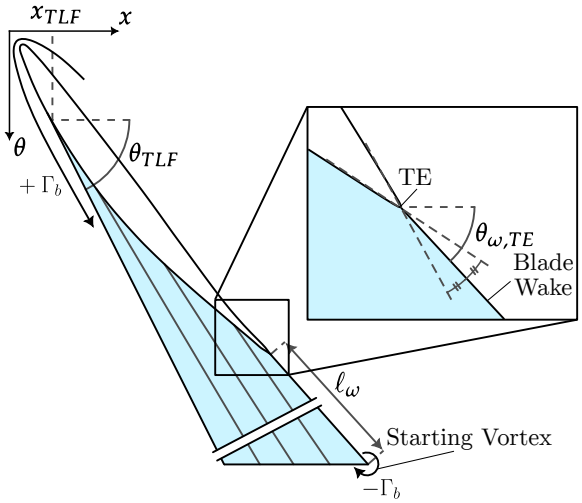

Figure 4. Parameters of the blade wake and TLF sheet geometries.

The TLF sheet detaches from the blade-tip suction-side edge and models the vorticity sheet of the TLF. It is defined by its axial detachment position x_{TLF} and pitch angle θ_{TLF} of the upstream row of panels, as shown in Figure 4. The pitch angle changes linearly over the subsequent panel rows until it aligns with the blade wake pitch angle at TE. The TLF panels match the point distribution of the blade wake, ensuring precise alignment of the panel rows at the TE. These x_{TLF} and θ_{TLF} parameters are iteratively refined during the calculation.

The position of the axial separation is found by identifying the point with the highest pressure difference between the two sides of the blade near the tip:

$$x_{TLF} = \text{argmax}\big(\Delta C_p(r/R = 87.5\%)\big) \tag{19}$$

This location is consistent with the experimental data from [27]. The arbitrary normalized radial position of 87.5% is close to the tip and at the same time minimizes the influence of the TLF of the blade load distribution [28]. Near the tip, the TLF causes a lower pressure

on the suction side, associated to the leakage flow. This leakage blocks the primary flow and increases the pressure near the LE.

The TLF pitch angle is computed from the mid-span average pressure difference, using a correlation from Chen et al. [29].

$$\theta_{TLF} = \arctan\left(0.46\sqrt{\frac{\left(\Delta C_p(r/R = 50\%)\right)_{avg}}{2}}\right) \tag{20}$$

This expression shown its reliability in various configurations.

Both x_{TLF} and θ_{TLF} depend on the blade pressure distribution, which in turn is affected by the blade wake and the TLF sheet positions. The iterative process is continued until convergence is reached on the parameters.

3. Results

3.1. Case study: LMFA NACA65 rotor

The NACA65 rotor rig is located at the Laboratoire de Mécanique des Fluides et d'Acoustique (LMFA), École Centrale de Lyon [30,31]. The shrouded fan operates at 1 500 rpm. It consists of a 12 blades rotor with a hub diameter of 196 mm and a shroud diameter of 317 mm . The blades are constituted with NACA 65 series profiles with a thickness of 9% of the chord. They have a circular camber line and are designed to maintain a constant outflow angle along the span. The chord length ranges from 166.7 mm at the hub to 151.5 mm at the tip. The tip clearance is 1.1% of the blade height, i.e. 1.3 mm. The inlet Mach number is about 0.1 and the Reynolds number based on the chord length is $5 \cdot 10^5$. As illustrated in Figure 5, two measurement planes are defined: P1 is at 18% c_{ax} from the LE and P2 is at 44% c_{ax} from the TE.

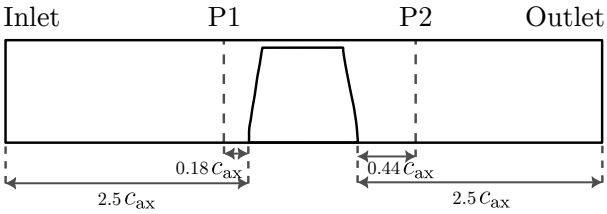

Figure 5. LMFA NACA65 rotor computational domain dimensions.

RANS simulations have been performed on a single sector to calibrate and validate the HPM. The domain was meshed using *Cadence AutoGrid5*, generating approximately $3.5 \cdot 10^6$ cells with a resolved boundary layer mesh that reaches $y^+ < 1$. The simulations used the *elsA* solver from ONERA [32]. The Roe scheme with second order spatial accuracy and the Kok $k - \omega$ turbulence model [33] have been employed. Periodic boundary conditions were defined at the azimuthal boundaries, while an adiabatic no-slip condition has been used on the walls. The inlet condition consists of a uniform axial flow. This choice the typical inlet condition for HPM. Radial equilibrium was applied at the outlet. Inlet and outlet are located 2.5 axial chords away from the blade. The convergence of the simulations was assessed by a decrease of the residuals by 4 orders of magnitude and a relative error of the mass flow rate below 0.1%.

Figure 6 shows the compressor map for the 1 500 rpm iso-speed, obtained from the RANS simulations. The operating point with the peak efficiency (PE) is selected for the verification and validation of the HPM results. This point stands for minimal losses and a low influence of secondary flows due to attached boundary layers. This choice is adapted to the HPM approach, which neglects the viscous losses, making the PE point ideal for validation.

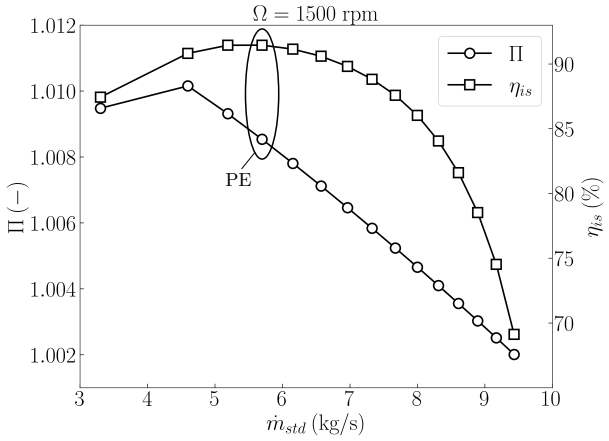

Figure 6. Compressor map of the LMFA NACA65 rotor at 1 500 rpm, from RANS simulations.

3.2. Verification for a shrouded rotor

3.2.1. Blade wake length

One parameter needs to be calibrated: the length of the blade wake, ℓ_ω, which determines the position of the starting vortex relative to the blade. This spanwise vortex line is located on the last panel row of the wake, which is furthest from the TE of the blade, as shown in Figure 4. According to Kelvin's circulation theorem, this vortex forms when the airfoil is set in motion and has an equal but opposite circulation to the airfoil. In panel methods, the starting vortex is usually positioned far away from the airfoil to reduce its influence. This placement is critical for external flow applications where the flow should return to the freestream far from the body. In the VLM, this is achieved by using horseshoe vortices where the starting vortex is assumed to be at an infinite distance [34]. In the panel method, a long wake is used [1], while unsteady approaches assess convergence by the reduction of the starting vortex influence when the wake length grows [9–11,18,35]. For shrouded rotors, the outlet flow is confined by the endwalls, so the wake length must be adjusted to impose the proper flow deflection downstream.

The HPM calculations are configured for a sector with periodic conditions. A mesh convergence analysis resulted in a mesh with 6 910 panels, including 5 706 collocation points. HPM simulations are performed with different wake lengths. The axial velocity is adjusted to match the RANS PE mass flow rate at the P1 inlet plane, keeping the relative error below 1%.

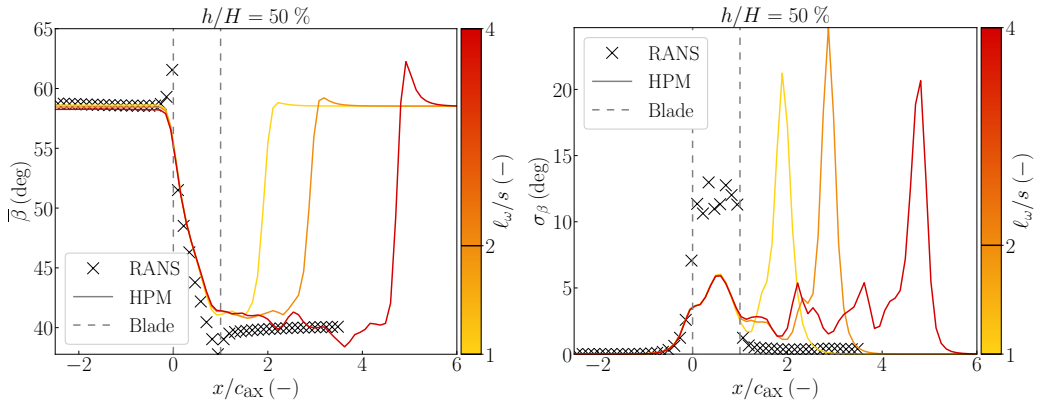

(a) Pitchwise average. **(b)** Pitchwise standard deviation.

Figure 7. Axial evolution of the relative flow angle, at mid-span, for different wake lengths.

Figure 7 illustrates how the wake length, measured as blade-to-blade pitch s, affects mid-span flow deviation. First, the axial evolution of the pitchwise-averaged relative flow angle is presented in Figure 7a, for three different values of ℓ_ω/s. The flow is deviated

by the blade and the resulting swirl is maintained down to the starting vortex. A good agreement is obtained with the RANS results. Downstream of the starting vortex, deviation cancels out to recover the upstream angle and satisfy the non-perturbation condition at infinity. The pitchwise standard deviation of the relative flow angle is shown in Figure 7b, to evaluate the azimuthal variations of the angle β. Artificially high values are found close to the starting vortex. Consequently, the starting vortex should be located sufficiently far to model the deviation in the region of interest and limit the pitchwise fluctuations. In the present case, a distance $\ell_\omega/s = 2$ is sufficient to extract the results at P2.

3.2.2. Blade wake slip condition

Figure 8 evaluates the slip condition error on the wake, for a wake length of two blade pitches. The normal velocity at the center of each wake panel is normalized by the relative freestream velocity. The frozen wake with the TE bisector trajectory leads to rather low normal velocities. In most panels, these velocities are less than 10% of the relative freestream velocity. Near the starting vortex, the slip condition is not fulfilled due to the vortex circulation. The error level is considered moderate. Iterative methods could reduce this error by adjusting the wake trajectory, but with a higher computational cost [14].

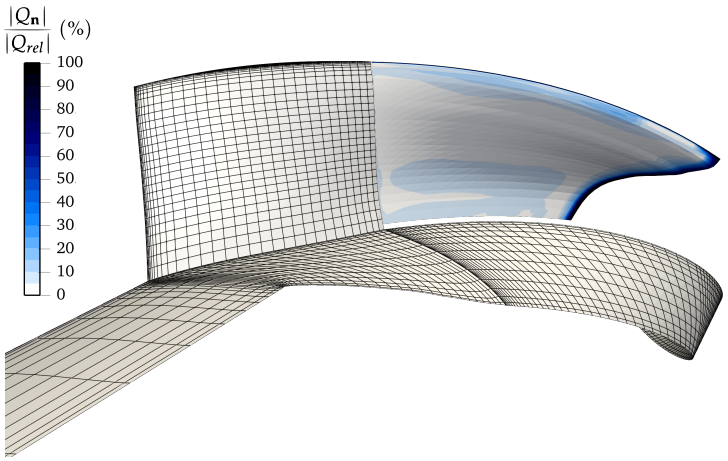

Figure 8. Slip condition error in the blade wake: normal velocity scaled with the relative freestream velocity.

3.2.3. Periodicity condition

The periodicity condition is verified by comparing two HPM calculations at the PE point. The first simulation uses a single sector with the periodicity condition and the same mesh as before. The second simulation covers the entire 360° rotor, with the mesh of the single sector replicated 12 times. Table 1 shows the comparison of the computational performance between the two cases. Both cases were executed on the same hardware with 16 threads.

Table 1. Performance comparison between single sector and full 360° HPM computations.

Simulation	Number of Panels	Execution Time [s]	Memory Usage [Go]
Sector	6 910	43	0.3
Full 360°	82 920	1 207	37.5

The calculation of the full 360° rotor takes 28 times longer than that of the single sector, and the memory requirement is 125 times higher. Figure 9 shows the spanwise distribution of the blade force coefficient c_z is in excellent agreement between the two calculations. This result validates the periodicity condition for HPM.

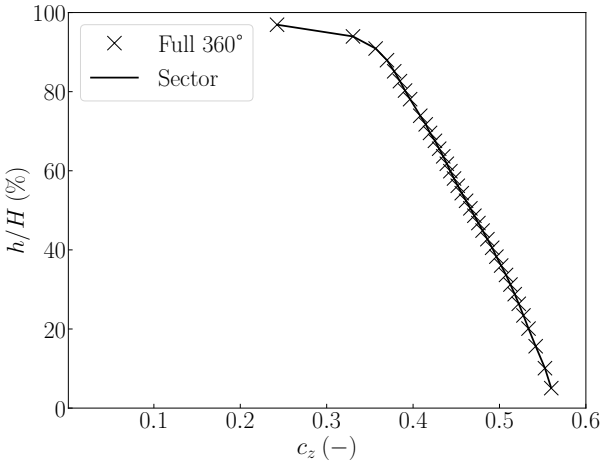

Figure 9. Spanwise evolution of the blade force coefficient for the sector and full 360° computations.

3.3. Validation

To validate the HPM, comparisons are made with RANS simulations at the PE point. Figure 10 shows the pressure coefficient distributions for the HPM and RANS at 25% , 50% and 87.5% of the blade height. The pressure coefficient for RANS is calculated using the equation:

$$C_p = \frac{p - p_{ref}}{\frac{1}{2}\rho_{ref} Q^2_{rel_{ref}}} \tag{21}$$

The reference values are derived from pitchwise averaged quantities at the LE [36]. The HPM results agree well with the RANS simulations at 25% and 50% of the blade height. At 87.5% of the blade height, it underestimates the pressure difference. The discrepancy may result from the approach of the frozen wake and TLF. It affects the blade loading, particularly near the TE and the tip, even if the error in the slip condition of the blade wake is minimal. In addition, as shown in Figure 13, the inviscid nature of the HPM does not account for the thickening boundary layer at the TE, especially near the tip. The corresponding increase in pressure difference between both sides of the blade, as shown by the RANS simulations, is not rendered.

As previously described, the TLF model uses the load distribution for the definition of the TLF sheet geometry. The mean value of ΔC_p at mid-span is used to calculate its pitch angle. Meanwhile, the maximum pressure difference between both sides at 87.5% blade height is used to determine the detachment position. At these positions, the HPM is close to the RANS simulation.

Figure 11 shows the spanwise evolution of the pitchwise force coefficient. The HPM results slightly underestimate the blade load compared to the RANS simulation, consistently with the observations on the pressure coefficient. However, the decrease in load with increasing radius is captured.

Figure 12 shows the radial evolution of the axial velocity and the relative flow angle, in the planes P1 and P2. HPM accurately reproduces the conditions at the inlet, and a fairly good prediction is obtained at the outlet. The radial evolutions are well captured, but some differences appear on the levels. This discrepancy can arise because viscous effects are not taken into account in the HPM. As a result, there is a lower blockage, which decelerates the flow. The slight error in the slip condition of the frozen blade wake can also reduce the deflection. In addition, there are post-processing errors caused by the interactions between the wake singularities and the P2 plane. As shown in Figure 13, if the post-processing points are too close to the edges of the wake singularities, this can lead to unphysical values. This situation also explains the error of 1.5% in the mass flow rate measured with HPM. However, these differences are within acceptable limits for a preliminary design tool.

Outside of the blade wakes, a good agreement is observed in Figure 13 between RANS and HPM.

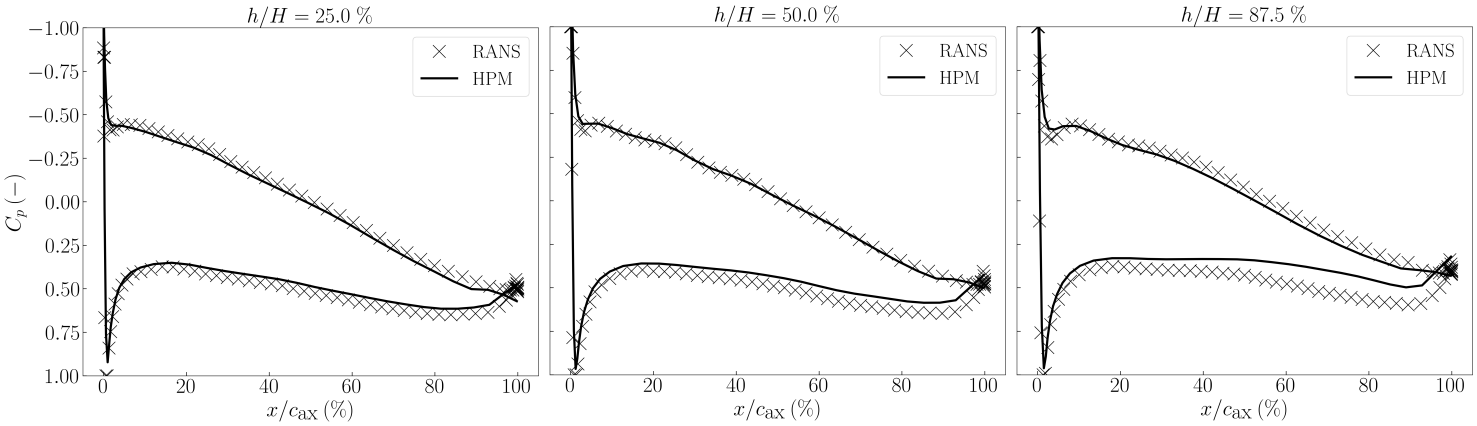

Figure 10. Chordwise distribution of the pressure coefficient at 25% (left), 50% (center) and 87.5% (right) of the blade height, comparing HPM and RANS simulations at PE point.

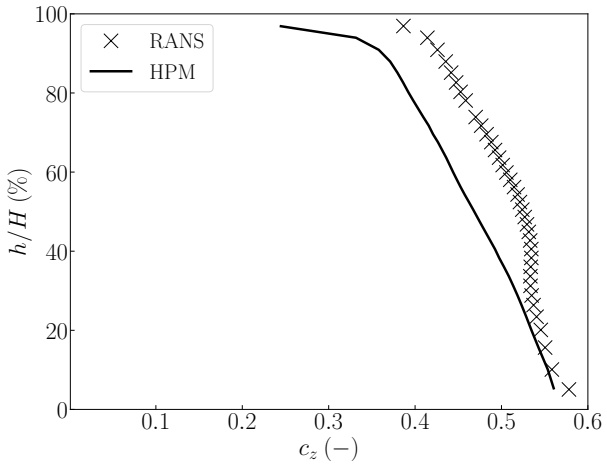

Figure 11. Spanwise evolution of the force coefficient, comparing HPM and RANS simulations at PE point.

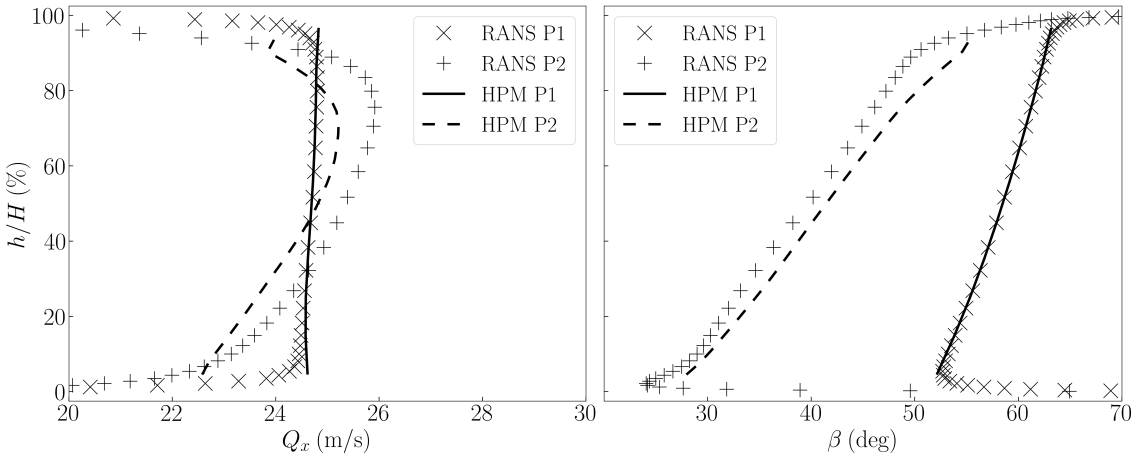

Figure 12. Spanwise evolution of the axial velocity (left) and the relative flow angle (right), in planes P1 and P2, comparing HPM and RANS simulations at PE point.

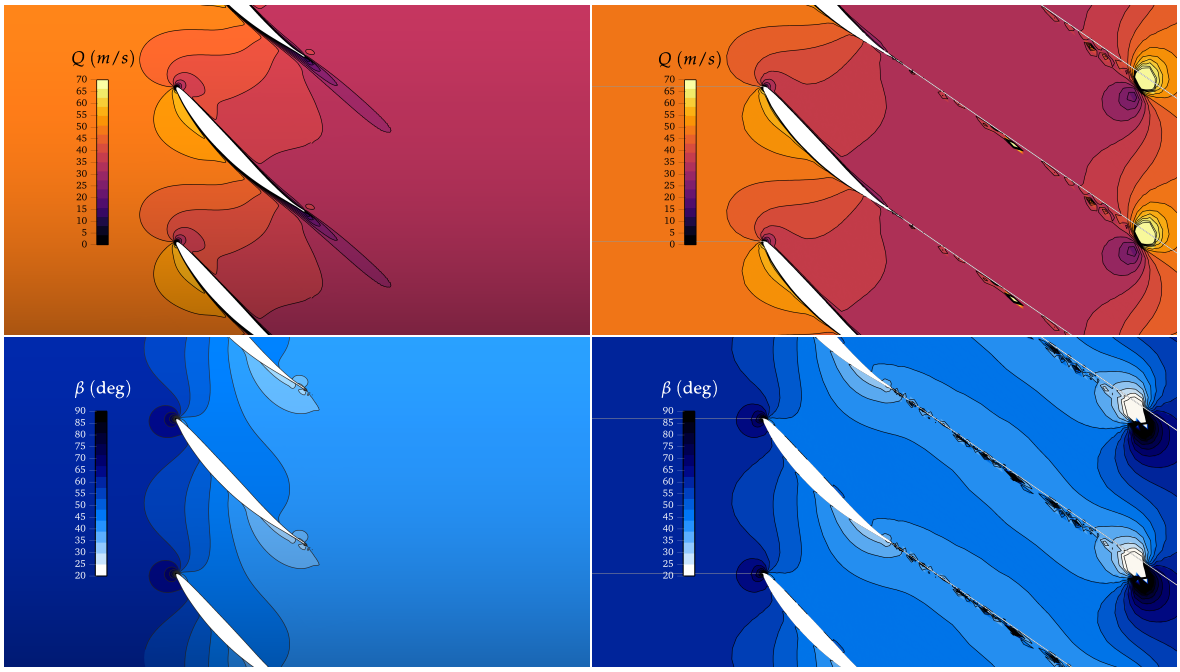

Figure 13. Blade-to-blade comparison of the velocity magnitude and the relative flow angle at mid-span: RANS simulation (left), HPM computation (right).

3.4. Sensitivity to operating point changes

An important focus when using low-order methods is to evaluate their ability to predict performance under different conditions. The HPM method is evaluated on several operating points in comparison with the RANS simulations introduced in Figure 6. The axial velocity is tuned to match the RANS mass flow rate at the P1 inlet, keeping the relative error below 1% at each point.

Figure 14 shows the radial evolution of axial velocity and relative flow angle at the P1 and P2 planes. HPM accurately replicates the upstream conditions. Downstream of the fan, a fairly good prediction is achieved, regarding both the radial evolutions and the levels. Moreover, the sensitivity to the mass flow rate is captured. However, the discrepancies increase with decreasing mass flow rate, which is directly related to the amplification of the viscous effects. Thinner boundary layers at higher mass flow rates reduce blockage, enhancing HPM coherence with RANS simulations. Conversely, lower mass flow rates amplify viscous effects and blockage, accelerating the flow in RANS simulations. Additional errors may result from the fact that the wake generation model does not account for local velocity changes under different operating conditions.

The spanwise evolution of the pitchwise force coefficient is plotted in Figure 15. The HPM results agree with the RANS simulations, although the load is predicted to be too low at lower mass flows. This is consistent with the previous observations: the higher axial velocity and flow deflection in the RANS simulations indicate a higher load. At higher mass flow rates, the HPM results are in better agreement with the RANS simulations. The evolution between the individual operating points is fairly well captured by HPM.

Figure 16 shows the detachment position and the pitch angle of the TLF at the last iteration of the HPM computations. The expected trends are observed [34], with the TLF pitch angle increasing as the mass flow rate decreases, while the detachment position moves upstream. Figure 17 compares the TLF shapes between RANS and HPM. For RANS, the TLF is identified by an iso-surface of the Q-criterion at $3 \cdot 10^7\ s^{-2}$. For HPM, the panel sheet is shown. At lower mass flow rates, HPM was shown to underestimate the blade loading, which leads to a smaller TLF pitch angle compared to RANS. However, the separation position is comparable in both cases. At higher mass flow rates, HPM effectively captures the TLF shape for the separation position and the pitch angle. This comparison shows

that the TLF model performs well at different operating points by capturing the expected trends.

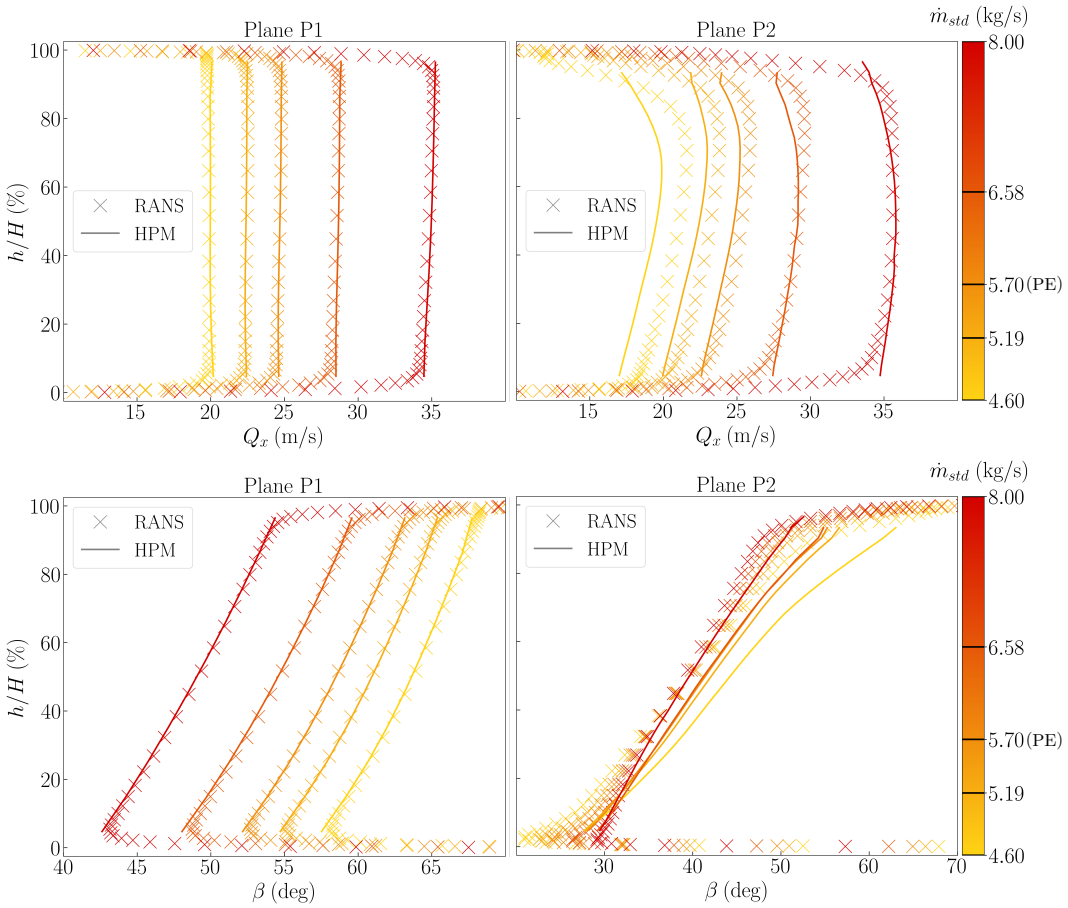

Figure 14. Radial evolution of the axial velocity and the relative flow angle, in planes P1 and P2, for different operating points.

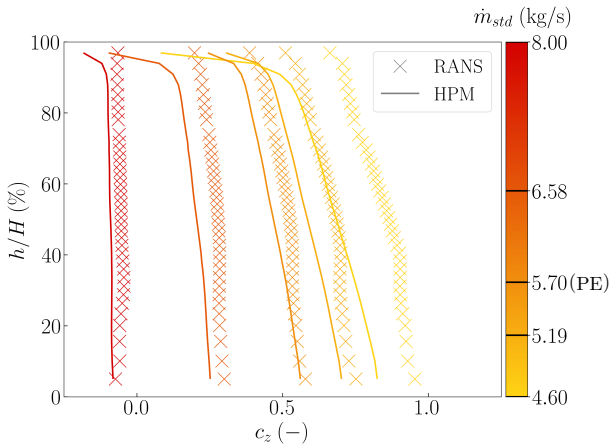

Figure 15. Spanwise evolution of the pitchwise force coefficient, for different operating points.

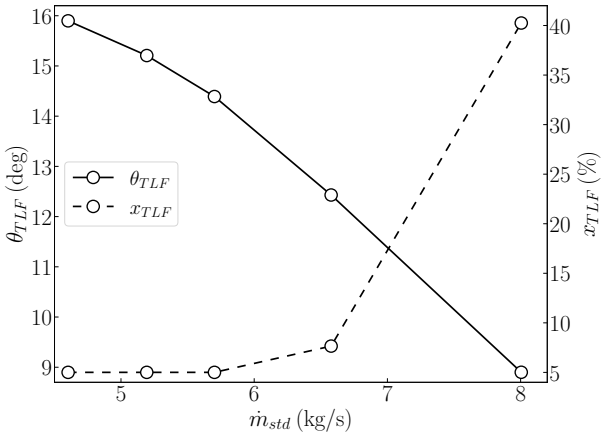

Figure 16. Evolution of the TLF detachment position and pitch angle, for different operating points, from HPM model.

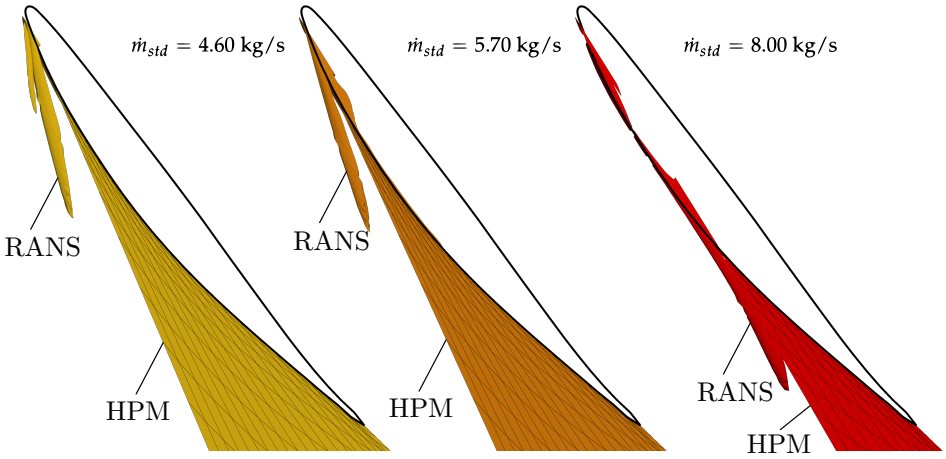

Figure 17. Comparison of the TLF shape between RANS (Q-criterion at $3 \cdot 10^7\ s^{-2}$) and HPM (TLF sheet), for different operating points.

4. Conclusions

A hybrid panel method has been introduced to predict the aerodynamic performance of shrouded fans. The method combines a vortex lattice method for the endwalls with a panel method for the blade, its wake and the TLF. The verification of the HPM was performed in comparison with RANS simulations of the LMFA NACA65 rotor at peak efficiency. For shrouded rotor flows, this study emphasizes the importance of the wake length for the correct prediction of flow deflection. The periodicity condition has been validated by comparing the results of a single sector with the full 360° rotor. An excellent agreement and a significant reduction in computational cost was observed. The HPM results agree well with the RANS simulation at peak efficiency. At different operating points, the two approaches show consistent behaviors in the flow field and blade loading. However, at lower mass flow rates, the HPM tends to underestimate the blade loading. The viscous blockage effect is not taken into account. Concerning the TLF, modelled by a panel sheet in the HPM, the main characteristics are in fairly good agreement between the two methods. The current frozen wake model limit the computational cost but introduces errors in the slip condition. Thus, future work will aim to implement a more accurate wake model [14]. Consideration of boundary layer effects could improve the predictions [1], and a diffusion model of the TLF could be investigated [11,12,34].

The HPM is a promising tool for the preliminary design of shrouded fans, as the computation times are less than one minute. Future research will apply the HPM to other

configurations with the aim of increasing the Mach number and taking into account the compressibility effects.

Author Contributions: Conceptualization, V.C., J.B. and E.L.; methodology, V.C., J.B. and E.L.; validation, V.C.; formal analysis, investigation, V.C.; writing—original draft preparation, V.C.; writing—review and editing, J.B. and E.L.; visualization, V.C.; supervision J.B. and E.L. All authors have read and agreed to the published version of the manuscript.

Funding: This research was funded by Safran Aircraft Engines, with support from the ANRT (Association Nationale Recherche Technologie) and the DGAC (Direction Générale de l'Aviation Civile) for the SONICE project.

Data Availability Statement: The raw data supporting the conclusions of this article will be made available by the authors on request.

Acknowledgments: The authors thank Safran Aircraft Engines (Safran Group) for permission to publish these results. This work was granted access to the HPC resources of PMCS2I (Pôle de Modélisation et de Calcul en Sciences de l'Ingénieur et de l'Information) of École Centrale de Lyon, Écully, France.

Conflicts of Interest: The authors declare no conflicts of interest.

Abbreviations

The following abbreviations are used in this manuscript:

HPM	Hybrid Panel Method
LE	Leading edge
PE	Peak efficiency
RANS	Reynolds-averaged Navier-Stokes
TE	Trailing edge
TLF	Tip-leakage flow
VLM	Vortex Lattice Method
$\mathbf{Q}$	Velocity vector
α	Absolute velocity pitchwise angle
β	Relative velocity pitchwise angle
φ	Velocity radial angle
$\mathbf{\Omega}$	Rotation speed
Φ	Velocity potential
σ	Source intensity
Γ	Circulation
μ	Doublet intensity
a	Vortex influence coefficient
b	Source influence coefficient
c	Doublet influence coefficient
$\mathbf{r}$	Panel radial coordinate vector
$\mathbf{n}$	Panel normal vector
c_{ax}	Axial chord length
s	Blade pitch
H	Blade height
ℓ_ω	Wake length
σ_{vc}	Vena contracta contraction coefficient
θ_{TLF}	Pitch angle of the TLF sheet
x_{TLF}	Axial detachment position of the TLF sheet
C_p	Pressure coefficient
ΔC_p	Pressure coefficient difference
c_z	Pitchwise force coefficient
N	Number of periodic sectors
n	Number of panels
$\cdot_\infty$	Free stream conditions
$\cdot_{rel}$	Relative frame of reference
$\cdot_{ew}$	Endwall
$\cdot_b$	Blade
$\cdot_\omega$	Wake
$\cdot_{TLF}$	TLF
$\cdot_{TE}$	Trailing edge
$\cdot_v$	Velocity formulation
$\cdot_p$	Potential formulation
$\cdot^\perp$	Projected onto the panel normal vector
$\cdot^*$	Corrected influence coefficient

References

1. Katz, J.; Plotkin, A. Low-Speed Aerodynamics, Second Edition. *Journal of Fluids Engineering* **2004**, *126*, 293–294. https://doi.org/10.1115/1.1669432.
2. Falkner, V.M. The Calculation of Aerodynamic Loading on Surfaces of Any Shape. *His Majesty's Stationery Office* **1943**.
3. Masquelier, M.L. Application of the Vortex-Lattice Method to Propeller Performance Analysis. PhD thesis, Air Force Institute of Technology, 1982.
4. Kobayakawa, M.; Onuma, H. Propeller Aerodynamic Performance by Vortex-Lattice Method. *Journal of Aircraft* **1985**, *22*, 649–654. https://doi.org/10.2514/3.45181.
5. Lesieutre, D.J.; Sullivan, J.P. The Analysis of Counter-Rotating Propeller Systems. In Proceedings of the General Aviation Aircraft Meeting and Exposition, 1985, pp. 564–575. https://doi.org/10.4271/850869.

6. Houten, R.V. Analysis of Ducted Propellers in Steady Flow. *Airflow Research And Manufacturing Corp* **1986**, p. 65.
7. McHugh, G.P. Advances in Ducted Propulsor Analysis Using Vortex-Lattice Lifting-Surface Techniques. PhD thesis, Massachusetts Institute of Technology, 1997.
8. Stubblefield, J.M. Numerically-Based Ducted Propeller Design Using Vortex Lattice Lifting Line Theory. PhD thesis, Massachusetts Institute of Technology. Department of Mechanical Engineering, 2008.
9. Fei, X.; Litherland, B.L.; German, B.J. Development of an Unsteady Vortex Lattice Method to Model Propellers at Incidence. *AIAA Journal* **2021**, pp. 1–13. https://doi.org/10.2514/1.J060133.
10. Colmenares, J.D.; López, O.D.; Preidikman, S. Computational Study of a Transverse Rotor Aircraft in Hover Using the Unsteady Vortex Lattice Method. *Mathematical Problems in Engineering* **2015**, *2015*, 1–9. https://doi.org/10.1155/2015/478457.
11. Proulx-Cabana, V.; Nguyen, M.T.; Prothin, S.; Michon, G.; Laurendeau, E. A Hybrid Non-Linear Unsteady Vortex Lattice-Vortex Particle Method for Rotor Blades Aerodynamic Simulations. *Fluids* **2022**, *7*, 81. https://doi.org/10.3390/fluids7020081.
12. Ahuja, V.; Hartfield, R.J. Aerodynamic Loads over Arbitrary Bodies by Method of Integrated Circulation. *Journal of Aircraft* **2016**, *53*, 1719–1730. https://doi.org/10.2514/1.C033619.
13. Ahuja, V.; Litherland, B.L. Comparison of Aerodynamic Analysis Tools Applied to a Propeller-Blown Wing **2023**.
14. Baltazar, J.; Falcão de Campos, J.A.C. On the Modelling of the Potential Flow About Wings and Marine Propellers Using a Boundary Element Method. PhD thesis, Technical University of Lisbon, 2008.
15. Baltazar, J.; Falcão de Campos, J.A.C. On the Modelling of the Flow in Ducted Propellers With a Panel Method. *First International Symposium on Marine Propulsors* **2009**.
16. Baltazar, J.; Falcão de Campos, J.A.C.; Bosschers, J. Open-Water Thrust and Torque Predictions of a Ducted Propeller System with a Panel Method. *International Journal of Rotating Machinery* **2012**, *2012*, 1–11. https://doi.org/10.1155/2012/474785.
17. Baltazar, J.; Rijpkema, D.; Falcão de Campos, J. A. C., J.; Bosschers, J. Prediction of the Open-Water Performance of Ducted Propellers with a Panel Method. *Journal of Marine Science and Engineering* **2018**, *6*, 27. https://doi.org/10.3390/jmse6010027.
18. Kim, S.; Kinnas, S.; Du, W. Panel Method for Ducted Propellers with Sharp Trailing Edge Duct with Fully Aligned Wake on Blade and Duct. *Journal of Marine Science and Engineering* **2018**, *6*, 89. https://doi.org/10.3390/jmse6030089.
19. Hamid, A. Unsteady Nonlinear Panel Method with Mixed Boundary Conditions. *FME Transactions* **2021**, *49*, 135–146. https://doi.org/10.5937/fme2101135A.
20. Ashby, D.L.; Sandlin, D.R. Application of a Low Order Panel Method to Complex Three-Dimensional Internal Flow Problems. Technical Report NASA-CR-177424, NASA, California Polytechnic State Univ. San Luis Obispo, CA, United States, 1986.
21. Hess, J.; Smith, A. Calculation of Potential Flow about Arbitrary Bodies. *Progress in Aerospace Sciences* **1967**, *8*, 1–138. https://doi.org/10.1016/0376-0421(67)90003-6.
22. Caries, V.; Montsarrat, C.; Boudet, J.; Lippinois, E. Vortex Lattice Method for Fan Tip-Flow Modeling. In Proceedings of the European Conference on Turbomachinery Fluid Dynamics and Thermodynamics, Budapest, Hungary, 2023. https://doi.org/10.29008/ETC2023-318.
23. Milne Thomson, L.N. *Theoretical Hydrodynamics*, 4th ed.; Universallibrary, The Macmillan And Company, 1962.
24. Moore, J.; Tilton, J.S. Tip Leakage Flow in a Linear Turbine Cascade. *Journal of Turbomachinery* **1988**, *110*, 18–26. https://doi.org/10.1115/1.3262162.
25. Montsarrat, C. Tip-leakage flow modelling in axial compressors. PhD thesis, Ecole Centrale de Lyon, Ecully, 2021.
26. Filkovic, D. Apame 3D Panel Method. http://www.3dpanelmethod.com/home.html, 2008.
27. Storer, J.A.; Cumpsty, N.A. Tip Leakage Flow in Axial Compressors. *Journal of Turbomachinery* **1991**, *113*, 252–259. https://doi.org/10.1115/1.2929095.
28. Ducharme, E.H. Velocity Scaled Aeroelastic Testing of an Unducted Fan. PhD thesis, Massachusetts Institute of Technology, 1987.
29. Chen, G.T.; Greitzer', E.M.; Tan', C.S.; Marble, F.E. Similarity Analysis of Compressor Tip Clearance Flow Structure **1990**.
30. Vouillarmet, A.; Charpenel, S. *Advanced Non-Intrusive Instrumentation for Propulsion Engines: Papers Presented at the Propulsion and Energetics Panel (PEP) 90th Symposium, Held in Brussels, Belgium, 20 - 24 October 1997 = (L'instrumentation Non-Invasive Avancée Pour Les Propulseurs)*; Number 598 in AGARD Conference Proceedings, AGARD: Neuilly-sur-Seine, 1998.
31. Charpenel, S. Caracterisation d'une Technique d'Anemometrie Laser Bipoint Tridimensionnelle L2F-3D pour l'Analyse de l'Ecoulement dans un Compresseur Axial Basse-Vitesse. PhD thesis, Ecole Centrale de Lyon, 1998.
32. Cambier, L.; Heib, S.; Plot, S. The Onera *elsA* CFD Software: Input from Research and Feedback from Industry. *Mechanics & Industry* **2013**, *14*, 159–174. https://doi.org/10.1051/meca/2013056.
33. Kok, J.C. Resolving the Dependence on Freestream Values for the k- Turbulence Model. *AIAA Journal* **2000**, *38*, 1292–1295. https://doi.org/10.2514/2.1101.
34. Montsarrat, C.; Boudet, J. Vortex Lattice Method Investigation of Tip-leakage Flow. *Journal of Turbomachinery* **2024**, pp. 1–14. https://doi.org/10.1115/1.4065897.
35. Katz, J.; Maskew, B. Unsteady Low-Speed Aerodynamic Model for Complete Aircraft Configurations. *Journal of Aircraft* **1988**, *25*, 302–310. https://doi.org/10.2514/3.45564.
36. Kravtsoff, F. Axial Compressor Modeling with CFD-based Throughflow and Potential Approach. PhD thesis, Ecole Centrale de Lyon, 2023.